



LAWRENCE
LIVERMORE
NATIONAL
LABORATORY

TEM Study of Oxide Nanoparticles in ODS Steels Developed for Radiation Tolerance

L. Hsiung, M. Fluss, J. Kuntz, B. El-Dasher, W.
Choi, S. J. Tumey, A. Kimura

October 19, 2009

2010 TMS Annual Meeting
Seattle, WA, United States
February 14, 2010 through February 18, 2010

Disclaimer

This document was prepared as an account of work sponsored by an agency of the United States government. Neither the United States government nor Lawrence Livermore National Security, LLC, nor any of their employees makes any warranty, expressed or implied, or assumes any legal liability or responsibility for the accuracy, completeness, or usefulness of any information, apparatus, product, or process disclosed, or represents that its use would not infringe privately owned rights. Reference herein to any specific commercial product, process, or service by trade name, trademark, manufacturer, or otherwise does not necessarily constitute or imply its endorsement, recommendation, or favoring by the United States government or Lawrence Livermore National Security, LLC. The views and opinions of authors expressed herein do not necessarily state or reflect those of the United States government or Lawrence Livermore National Security, LLC, and shall not be used for advertising or product endorsement purposes.

TEM Study of Oxide Nanoparticles in ODS Steels Developed for Radiation Tolerance

Luke L. Hsiung¹, Michael J. Fluss¹, Joshua D. Kuntz¹,
Bassem S. El-Dasher¹, B. William Choi¹, Scott J. Tumey¹, Akihiko Kimura²

¹Lawrence Livermore National Laboratory
Physical and Life Sciences Directorate
L-352, P.O. Box 808
Livermore, CA, U.S.A.

²Institute of Advanced Energy
Kyoto University, Gokasho, Uji
Kyoto 611-0011, Japan

Keywords. HRTEM, ODS steels, oxide nanoparticles, interfaces, core/shell structure

Introduction

Development of high-performance structural materials for first wall and breeding-blanket components, which will be exposed to high fluxes of high energy (14 MeV) neutrons from the deuterium-tritium fusion, is one of the major challenges in materializing future fusion/fission hybrid reactors. The choice of structural materials for the first wall and blanket to a large degree dictates the design of the hybrid reactor systems. The selection of suitable structural materials is based on conventional properties (such as thermophysical, mechanical, and corrosion and compatibility), low neutron-induced radioactivity, and resistance to radiation-induced damage phenomena like material hardening/embrittlement and/or dimensional instability caused by void- and helium-driven swelling [1]. Reduced activation ferritic/martensitic (F/M) steels possess modified compositions of commercial ferritic/martensitic steels by exchanging Mo, Nb, and Ni with W, V, and Ta for low long-term induced radioactivity have been selected as one of the primary candidate structural materials for fusion reactor applications because of their high thermal conductivity, good resistance to radiation-induced swelling, and helium-induced embrittlement in experimental tests. The service temperature capability of reduced activation F/M steels is, however, limited to around 600 °C because of their inferior tensile and creep strength at high temperatures. Oxide dispersion strengthened (ODS) F/M and ferritic steels produced by mechanical alloying (MA) of elemental or pre-alloyed powders of metallic matrix complemented with an adequate quantity of yttria (Y₂O₃) powder consolidated by hot extrusion or hot isostatic pressing are advanced structural materials with a potential to be used at elevated temperatures due to the dispersion of thermally stable oxide nanoparticles into the ferritic/martensitic matrix. The use of ODS steels should improve creep strength and oxidation/corrosion resistance at high temperatures

and consequently increase the operating temperature of first wall and blanket structures in the future fusion/fission hybrid reactors by at least 100 °C to approximately 700 °C or higher [2]. Significant progress has been made for the last few decades to understand the processing-microstructure-property relationships for ODS ferritic/martensitic steels, which led to the development of materials with exceptional high-temperature microstructural stability and creep strength coupled with effective trapping of transmutation gases. However, several key issues remain unsolved that include incomplete understanding of the effect of irradiation on low-temperature fracture properties, the role of fusion relevant helium and hydrogen transmutation gases on the deformation and fracture of irradiated material, radiation-induced solute segregation and phase stability, and mechanisms of swelling suppression in ODS steels [3]. To help resolving these issues, we are conducting HRTEM studies in order to further understand processing-structure-property relationships of ODS steels. The results obtained from HRTEM characterization of nanoparticles in ODS steels fabricated by mechanical alloying and hot extrusion processes are reported here.

Experimental

The materials used for this investigation were Fe-20Cr-4.5Al-0.34Ti-0.5Y₂O₃ (MA956) and Fe-16Cr-4Al-2W-0.3Ti-0.3Y₂O₃ (K3) ODS ferritic steels. Details of the fabrication process of the ODS steels can be found elsewhere [4, 5]. Briefly, the pre-alloyed powder was first mechanically alloyed with Y₂O₃ powder in an Argon gas atmosphere at room temperature using an attrition type ball mill. The powder was then sealed in a stainless-steel can and degassed at 400 °C in 0.1 Pa vacuum. The canned powders were subsequently consolidated by a hot extrusion technique at 1150 °C. After the extrusion, the consolidated ODS steel was thermally treated at 1050 °C for 1 hour. One K3-ODS steel sample was also annealed at 900 °C for 168 hours (one week) for

a study of the stability of nanoparticles. Thin foils for TEM analysis were prepared by a standard procedure that includes slicing, grinding, and polishing the recovered fragments with the foils surface approximately perpendicular to the loading axis. Final thinning of the foils was performed using a standard twin-jet electropolishing technique in an electrolyte (90 vol.% acetic acid, 10 vol.% perchloric acid) at 30 V and room temperature. Microstructural characterization was performed using Phillips CM300 field-emission transmission electron microscope (accelerating voltage of 300 kV). A software package CaRIne Crystallography 3.1 was used to simulate electron diffraction patterns in order to identify the crystal structures of ODS nanoparticles.

Results and discussion

Microstructures of K3 and MA956 ODS steels

Typical microstructures of the K3 and MA956 ODS steels are shown in Figs. 1a-1b and Figs. 1c-1d, respectively. Here, elongated grains (Fig. 1a) and dense oxide nanoparticles (Fig. 1b), mainly $Y_4Al_2O_9$ (YAM) complex oxide, were observed in K3-ODS steel. Elongated grains and $Y_4Al_2O_9$ oxide nanoparticles were also observed in MA956-ODS steel, as shown in Figs. 1a and 1b, except that the particles density in MA956-ODS is much lower than that in K3-ODS. The nanoparticle sizes in K3-ODS (Fig. 1b) are typically ranging from 1.5 nm to 30 nm, with a mean particle size of ~ 6 nm, and with a particle density on the order of $\sim 1.3 \times 10^{22} \text{ m}^{-3}$. Whereas the nanoparticle sizes in MA956-ODS (Fig. 1d) are typically ranging from 2 nm to 30 nm, the mean particle size is ~ 10 nm, and the particle density is on the order of $\sim 1 \times 10^{20} \text{ m}^{-3}$. $Y_4Al_2O_9$ has a monoclinic structure and space group: $P2_1/c$ with $a = 0.7375$ nm, $b = 1.0507$ nm, $c = 1.1113$ nm, and $\beta = 108.58^\circ$ [6, 7]. Here the orientation relationship between $Y_4Al_2O_9$ oxide phase and the matrix can be derived from the selected-area diffraction pattern: $(0\bar{1}1)_\alpha \parallel (2\bar{4}2)_{YAM}$ and $[011]_\alpha \parallel [432]_{YAM}$. The formation of $Y_4Al_2O_9$ oxide particles in both ODS steels was identified and confirmed by matching several observed and simulated diffraction patterns of different zone axes, and an example is shown in Fig.

2 for the $[432]_{YAM}$ -zone pattern. Their formation reveals the occurrence of an internal oxidation reaction: $2Y_2O_3 + Al_2O_3 \rightarrow Y_4Al_2O_9$ during consolidation that is governed by the oxygen affinity of different alloying elements. These results reveal that the formation of Y-Al complex oxides becomes predominant when ODS steels contain both Al and Ti, which is in agreement with a conclusion made by Kasada et al [8]. By comparing the $Y_4Al_2O_9$ nanoparticles formed in the ODS steel with the starting Y_2O_3 particles (space group: Ia_3 , a cubic structure with $a_0 = 1.06$ nm [7], particle size: 15-30 nm [9]) used to fabricate the ODS steel, one would realize that the formation of oxide nanoparticles in ODS steels does not take place solely through a fragmentation mechanism. Complex mechanisms involving fragmentation, dissolution of Y_2O_3 particles, and precipitation of complex-oxide nanoparticles were previously proposed by Okuda and Fujiwara [10], Kimura et al. [11] and Sakasegawa et al. [12] based on the results generated from x-ray diffraction and conventional TEM studies. However, recent studies conducted by Marquis [13] using 3-D atom probe method and Klimiankou et al. [14] using EDX and EELS methods have revealed the existence of a complex-oxide core structure associated with a solute-enriched shell structure in nanoparticles. The existence of core/shell structures in nanoparticles however challenges the accountability of previously proposed dissolution/precipitation mechanisms. HRTEM study of nanoparticles in K3-ODS was thus conducted to examine the interfacial structure of nanoparticles. Important results are displayed below so as to rationalize the formation of core/shell structures in oxide nanoparticles. Since K3-ODS steel contains 0.08 wt.%C, the formation of carbides in the steel is expected. Typical observations are shown in Fig. 3 together with a selected-area diffraction pattern of the $[112]_{Cr_{23}C_6}$ -zone. Here two inter-granular $Cr_{23}C_6$ (fcc, $a_0 = 1.064$ nm) carbides, one with a dimension of 650 nm long and 100 nm wide, can be readily seen. Notice that the streaks formed on the selected-area diffraction pattern are presumably caused by the existence of stacking faults in the carbide.

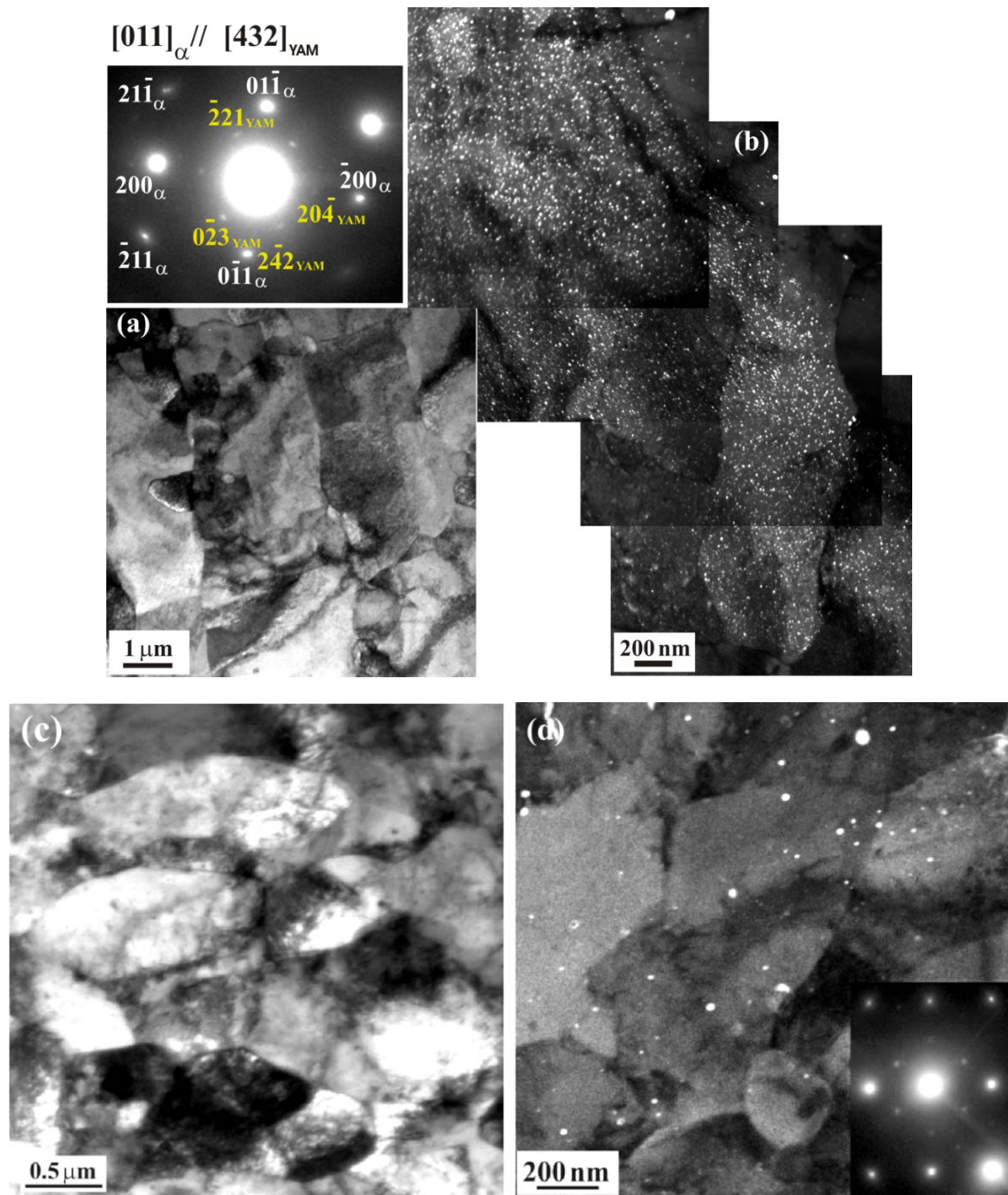


Fig. 1. (a) Bright-field TEM image shows typical grain morphology of K3-ODS steel, (b) dark-field TEM image and selected-area diffraction pattern of the $[011]_{\text{Fe-Cr}(\alpha)} \parallel [432]_{\text{YAM}}$ -zone show the formation of dense $\text{Y}_4\text{Al}_2\text{O}_9$ nanoparticles in K3-ODS steel, (c) bright-field TEM image shows typical grain morphology of MA956-ODS steel, (d) dark-field TEM image and selected-area diffraction pattern of the $[011]_{\text{Fe-Cr}(\alpha)} \parallel [432]_{\text{YAM}}$ -zone show the formation of $\text{Y}_4\text{Al}_2\text{O}_9$ nanoparticles in MA956-ODS steel.

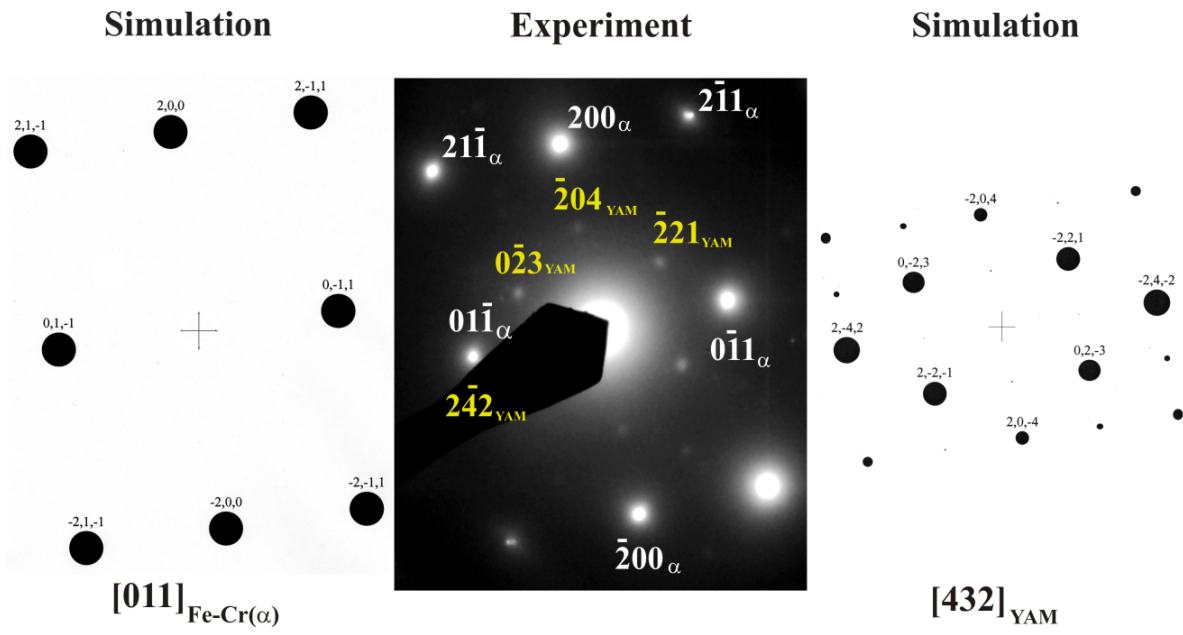


Fig. 2. Observed and simulated diffraction patterns of $[011]_{\text{Fe-Cr}(\alpha)}$ -zone and $[432]_{\text{YAM}}$ -zone for identifying the formation of $\text{Y}_4\text{Al}_2\text{O}_9$ complex-oxide nanoparticles.

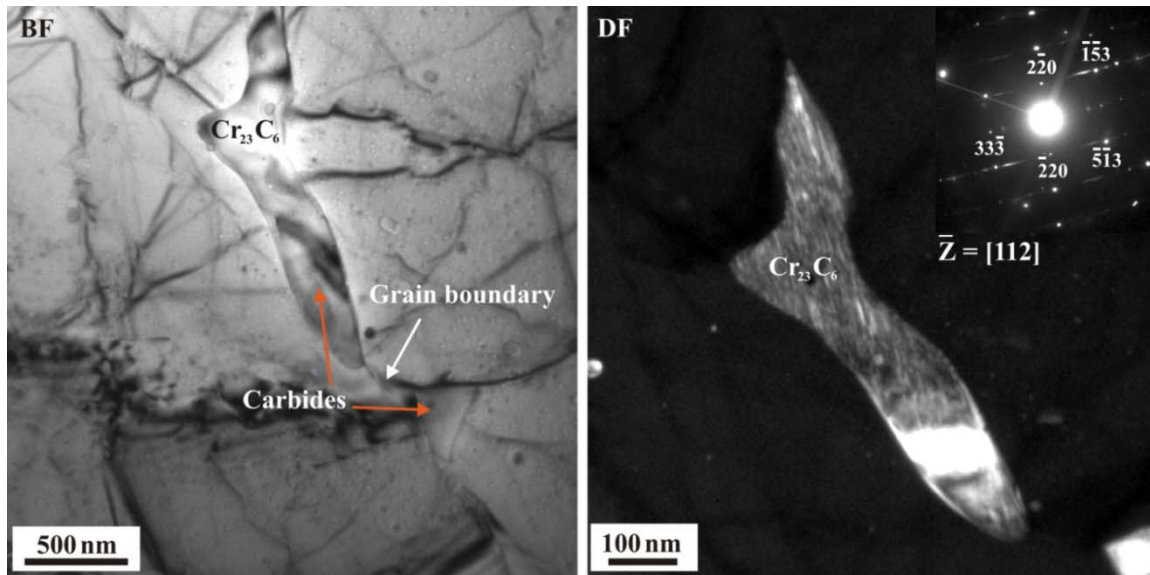


Fig. 3. Bright-field and dark-field TEM images and a selected-area diffraction pattern show the formation of intergranular Cr_{23}C_6 carbide in K3-ODS steel.

Structures and formation mechanisms of oxide nanoparticles

HRTEM images of a large (> 20 nm) and two small (< 10 nm) nanoparticles observed from a K3-ODS steel sample are shown in Figs. 4a, 4b and 4c. As can be seen in Fig. 4a, the large nanoparticle tends to be near spherical in shape and is incoherent with the matrix. In addition, we can also distinguish the core region with an appearance of lattice fringes from the outer shell region with a featureless appearance (presumably

due to amorphization that will be discussed below), although the shell region does not appear to have a uniform thickness. On the other hand, ledges and facets can be seen at the oxide/matrix interfaces of these two small nanoparticles, which tend to be coherent or semi-coherent with the matrix. Detail analysis of the small nanoparticle in Fig. 4b is shown in Fig. 5. Orientation relationship between the nanoparticle and the matrix can be derived from the fast Fourier transformation (FFT) image: $(0\bar{1}1)_\alpha \parallel$

$(004)_{YAM}$ and $[011]_{\alpha} \parallel [100]_{YAM}$. A large coherent strain (30%) can be generated if the oxide/matrix interface is coherent. However, the coherency strain can be reduced by inserting misfit dislocations at the interface to form semi-coherent interface. Detail analysis of the small nanoparticle in Fig. 4c is shown in Fig. 6. In addition to facets and ledges, interface dislocations and small featureless domains (marked by red arrows) can be seen at the oxide/matrix interface. Here a relatively smaller coherent strain (7%) is generated if the interface is fully coherent. Orientation relationship between the nanoparticle and the matrix, which is different from that in Fig. 5, can be derived from the FFT image: $(\quad)_{\alpha} \parallel (11)_{YAM}$ and $[011]_{\alpha} \parallel [732]_{YAM}$. Figure 7 provides an explanation why featureless domains in the outer shells of nanoparticles (shown in Figs. 4a and 6) form. Here nucleation of

crystalline $Y_4Al_2O_9$ domain (2 x 5 nm in size) can be seen within a partially crystallized particle. In addition, several arrays of atoms can be found to align parallel to the $(0\ 3)_{YAM}$ plane within the featureless amorphous domain on the left hand side of the particle. An interfacial structure similar to that shown in Fig. 6 can be found at the interface between the $Y_4Al_2O_9$ oxide and matrix. Orientation relationship between $Y_4Al_2O_9$ oxide and the matrix, which is different from those in Figs. 5 and 6, can be derived from the FFT image: $(0\ 1)_{\alpha} \parallel (2\ 2)_{YAM}$ and $[011]_{\alpha} \parallel [432]_{YAM}$. Thus, altogether three different orientation relationships were found between $Y_4Al_2O_9$ nanoparticle and the matrix. Clearly, the $\{011\}$ planes of the matrix act as habit planes for the nucleation of $Y_4Al_2O_9$ nanoparticles.

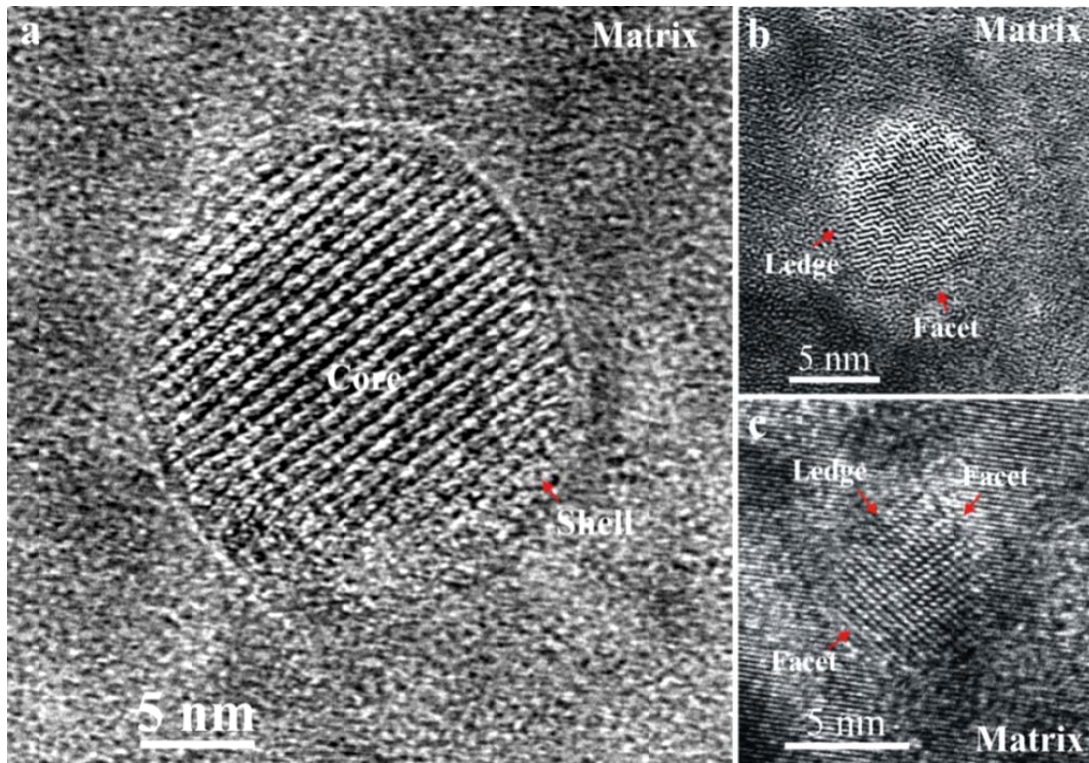


Fig. 4. HRTEM images of (a) a large nanoparticle (> 20 nm): incoherent interface associated with a core/shell structure and (b, c) small nanoparticles (< 10 nm): semi-coherent interfaces associated with facets and ledges.

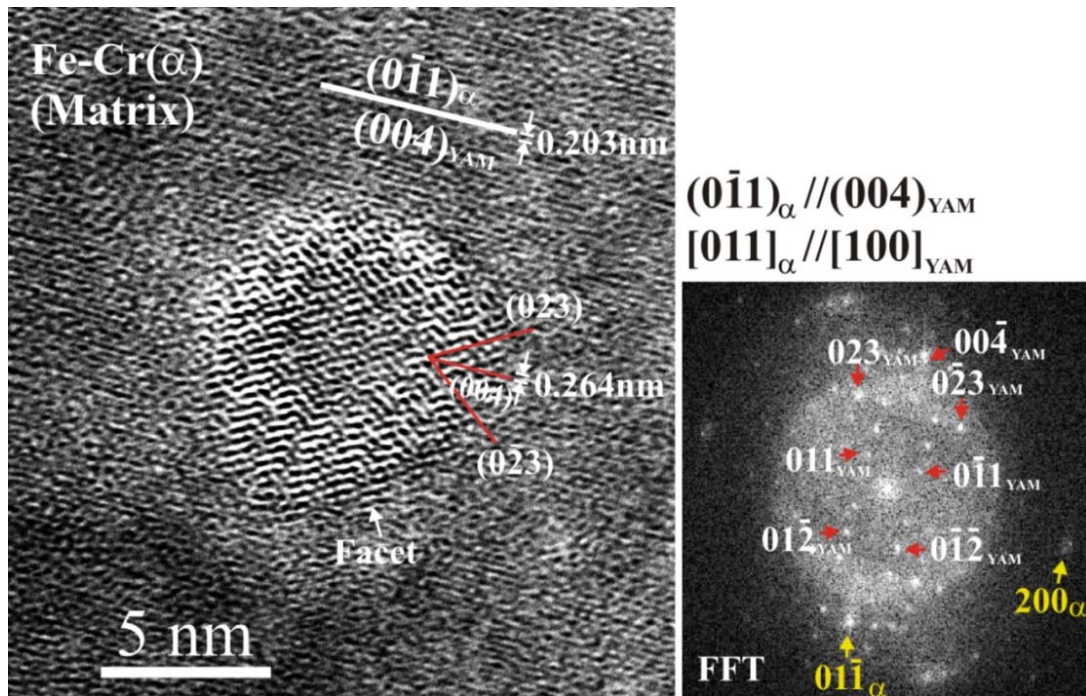


Fig. 5. HRTEM image shows the faceted interface between the small nanoparticle and matrix in Fig. 4b. Orientation relationship between $Y_4Al_2O_9$ nanoparticle and the matrix can be derived from the FFT image.

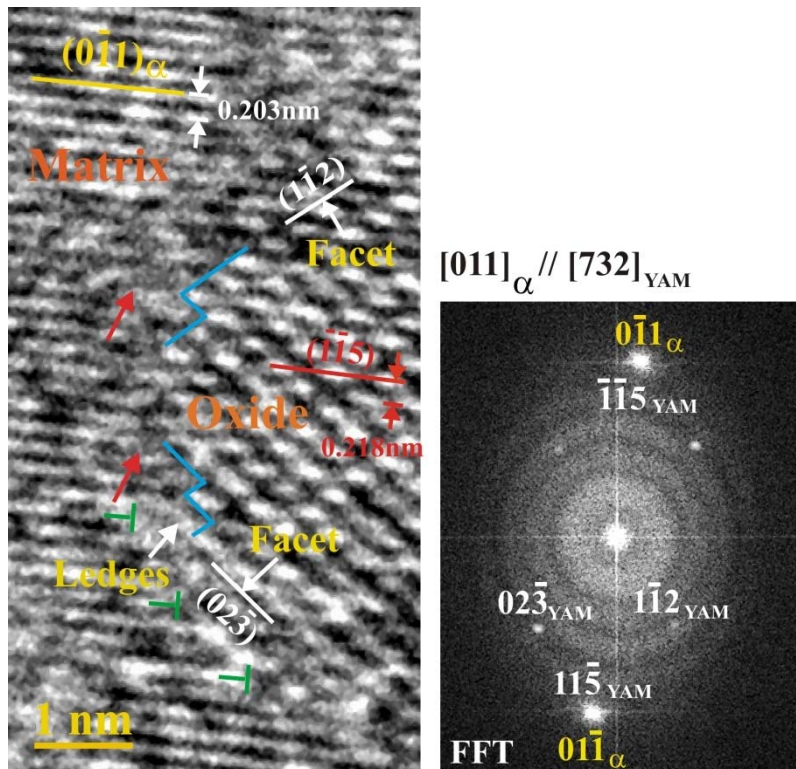


Fig. 6. HRTEM image shows the interfacial structure of the nanoparticle in Fig. 4c; facets, ledges, dislocations, and thin shell of featureless domains (marked by red arrows) can be found at the interface. Orientation relationship between $Y_4Al_2O_9$ nanoparticle and the matrix can be derived from the FFT image.

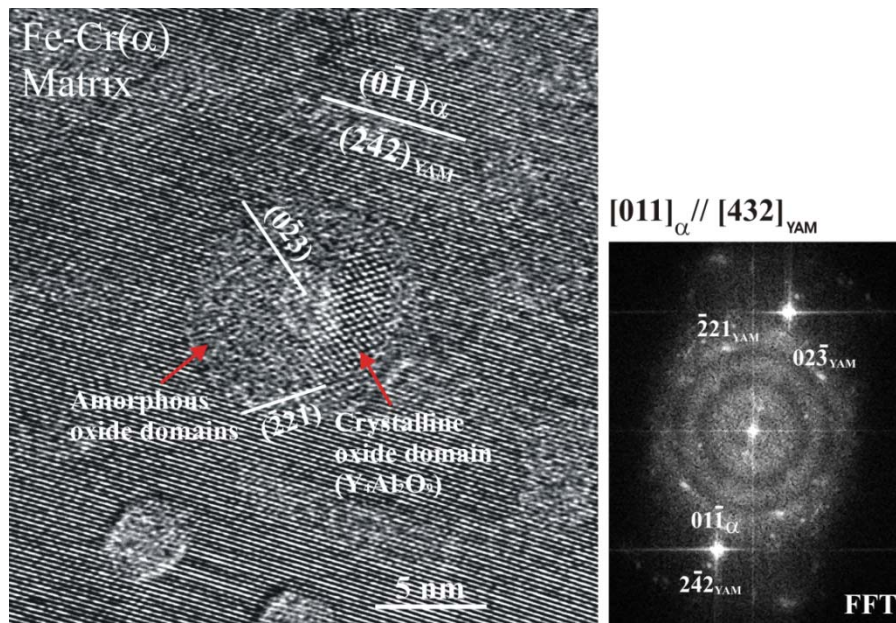


Fig. 7. HRTEM image shows nucleation of a crystalline $Y_4Al_2O_9$ domain (2 x 5 nm) in an amorphous particle; Orientation relationship between the $Y_4Al_2O_9$ crystal and the matrix can be derived from the FFT image.

Formation mechanisms of ODS nanoparticles are accordingly proposed based on the above HRTEM observations, which should include the following three stages: (1) Fragmentation of starting Y_2O_3 particles during ball milling; (2) Agglomeration and amorphization of fragmented oxide particles mixed with the matrix material during ball milling; (3) Crystallization of the amorphous oxide particles to form oxide nanoparticles with a complex-oxide core and a solute-enriched shell. The contents of complex-oxide core and solute-enriched shell are dependent on the compositions of different ODS steels. Y-Al complex-oxide core can form in Al-contained ODS steels, Y-Ti complex-oxide core can form in Ti-contained ODS steels with no addition of Al, and Y_2O_3 core can form in ODS steels with no additions of Al and Ti. The solute-enriched shell can be perceived as a result of the depletion of the solutes that are not involved in the oxidation reactions for the complex-oxide core. The shell thickness, which may not be uniform, is dependent on the size of nanoparticles since the larger the particle the more matrix material may participate in the agglomeration and amorphization stage and thus more solutes may be depleted from the oxide core during the crystallization stage. A solute-enriched shell forms when solute depletion rate from the core is greater than solute diffusion rate from the oxide/matrix interface during the crystallization stage. Figure 8 shows the result of an ODS steel sample annealed at 900 °C for 168 hours.

Here a perfectly spherical $Y_4Al_2O_9$ nanoparticle without a core/shell structure was observed as a result of the prolonged annealing, which seems to suggest that the core/shell structures of oxide nanoparticles formed in the as-fabricated ODS steels are far from chemical equilibrium.

Conclusion

The oxide nanoparticles formed in K3 and MA956 ODS steels are mainly $Y_4Al_2O_9$ (YAM) with a monoclinic structure. The interfacial structures of nanoparticles in K3-ODS steel have been investigated using HRTEM imaging techniques. Large nanoparticles (> 20 nm) usually have a spherical shape and tend to be incoherent with the matrix; small nanoparticles (< 10 nm) usually accompany with facets and ledges at the oxide/matrix interfaces and tend to be coherent or semi-coherent with the matrix. A structure of $Y_4Al_2O_9$ oxide core associated with amorphous shell forms in both large and small nanoparticles in the as-fabricated ODS steel sample. The core/shell structure disappears after prolonged annealing at 900 °C for 168 hours, which suggests that the core/shell structure of oxide nanoparticles is far from chemical equilibrium, it forms as a result of the crystallization of amorphous oxide particles generated during the mechanical alloying process.

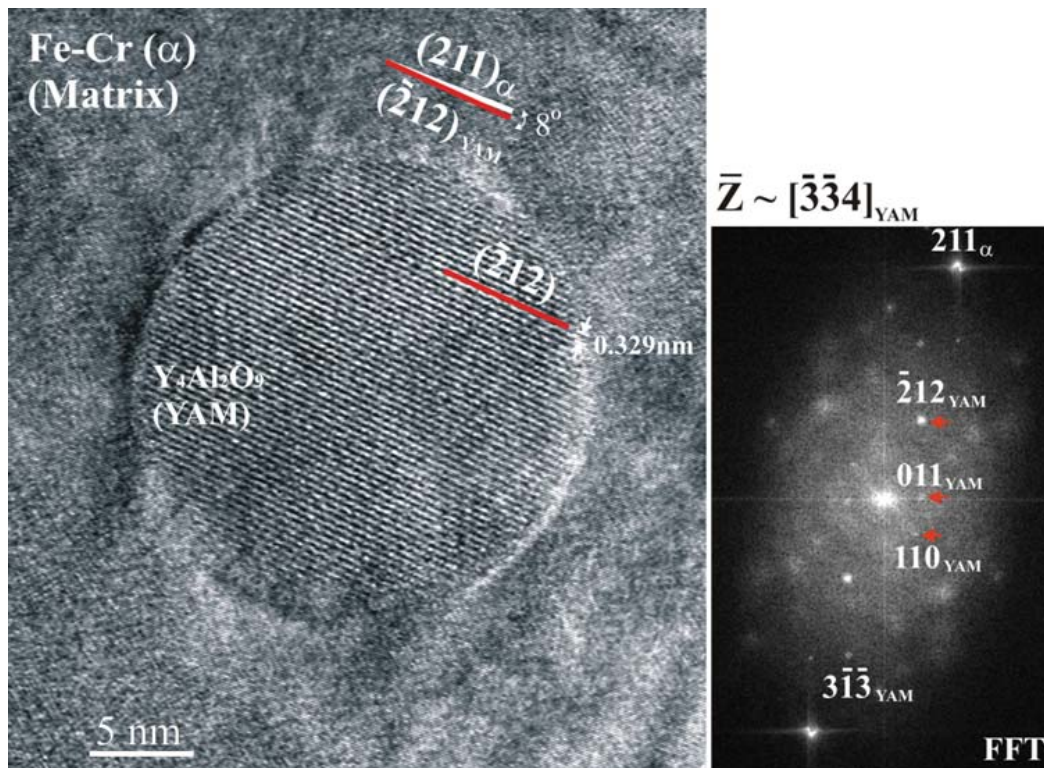


Fig. 8. HRTEM image of a large $Y_4Al_2O_9$ nanoparticle (> 20 nm) in an ODS steel sample after prolonged annealing at 900 °C for 168 hours. The nanoparticle becomes perfectly spherical without a core/shell structure.

Acknowledgements

This work was performed under the auspices of the U.S. Department of Energy by Lawrence Livermore National Laboratory under Contract DE-AC52-07NA27344. Work at LLNL was funded by the Laboratory Directed Research and Development Program at LLNL under project tracking code 09-SI-003. The authors gratefully acknowledge Nick E. Teslich and Rick J. Gross for their efforts on TEM sample preparation.

References

1. K. Ehrlich, Phil. Trans. R. Soc. Lond. A 357 (1999) 595.
2. S. Ukai, M. Fujiwara, J. Nucl. Mater. 307-311 (2002) 749.
3. E.E. Bloom, J.T. Busby, C.E. Duty, P.J. Maziasz, T.E. McGreevy, B.E. Nelson, B.A. Pint, P. F. Tortorelli, S.J. Zinkle, J. Nucl. Mater. 367-370 (2007) 1.
4. S. Uki, T. Nishida, H. Okada, T. Okuda, M. Fujiwara, K. Asabe, J. Nucl. Sci. Technol. 34 (3) (1997) 256.
5. S. Uki, T. Nishida, T. Okuda, T. Yoshitake, J. Nucl. Sci. Technol. 35 (4) (1998) 294.
6. A. Nørslund Christensen and R.G. Hazell, Acta Chemica Scandinavica 45 (1991) 226.
7. W.Y. Ching, Y.N. Xu, Physical Review B 59 (20) (1999) 12815.
8. R. Kasada, N. Toda, K. Yutani, H.S. Cho, H. Kishimoto, A. Kimura, J. Nucl. Mater. 367-370 (2007) 222.
9. V. de Castro, T. Leguey, M.A. Monge, A. Munoz, R. Pareja, D.R. Amador, J.M. Torralba, M. Victoria, J. Nucl. Mater. 322 (2003) 228.
10. T. Okuda, M. Fujiwara, J. Mater. Sci. Lett. 14 (1995) 1600.
11. Y. Kimura, S. Takaki, S. Suejima, R. Uemori, H. Tamehiro, ISIJ International, 39 (2) (1999) 176.
12. H. Sakasegawa, M. Tamura, S. Ohtsuka, S. Ukai, H. Tanigawa, A. Kohyama, M. Fujiwara, J. Alloys & Compounds 452 (2008) 2.
13. E. A. Marquis, Appl. Phys. Lett. 93 (2008) 181904.
14. M. Klimiankou, R. Lindau, A. Möslang, J. Nucl. Mater. 386-388 (2009) 553.